Peptide stereochemistry effects from pKa-shift to gold nanoparticle templating in a supramolecular hydrogel.

Simone Adorinni[†], Serena Gentile[†], Ottavia Bellotto[†], Slavko Kralj[∫], Evelina Parisi[†], Maria C. Cringoli[†], Caterina Deganutti[†], Giuliano Malloci[‡], Federica Piccirilli[⊥,⁞], Paolo Pengo[†], Lisa Vaccari[⊥], Silvano Geremia[†], Attilio V. Vargiu[‡], Rita De Zorzi[†]*, and Silvia Marchesan[†⁋]**

Dedicated to Professor Paolo Scrimin for his retirement

†Chem. Pharm. Sc. Dept., University of Trieste, 34127 Trieste, Italy

‡ Physics Dept., University of Cagliari, 09042 Monserrato (CA), Italy

∫Materials Synthesis Dept., Jožef Stefan Institute, 1000 Ljubljana, Slovenia

‖ Dept. of Pharmaceutical Technology, Faculty of Pharmacy, University of Ljubljana, 1000 Ljubljana, Slovenia

⊥ Elettra Sincrotrone Trieste, 34149 Basovizza, Italy

⁞ Area Science Park, 34149 Basovizza, Italy

⁋ INSTM, Unit of Trieste, 34127 Trieste, Italy

KEYWORDS. Peptides, self-assembly, hydrogels, chirality, gold nanoparticles, pKa.

ABSTRACT. The divergent supramolecular behavior of a series of tripeptide stereoisomers was elucidated through spectroscopic, microscopic, crystallographic and computational techniques. Only two epimers were able to effectively self-organize into amphipathic structures, leading to supramolecular hydrogels or crystals, respectively. Despite the similarity between the two peptides' turn conformations, stereoconfiguration led to different abilities to engage in intramolecular hydrogen bonding. Self-assembly further shifted the pKa of the C-terminal side chain. As a result, across the pH range 4-6, only one epimer predominated sufficiently as a zwitterion to reach the critical molar fraction allowing gelation. By contrast, the differing pKa values and higher dipole moment of the other epimer favored crystallization. The four stereoisomers were further tested for gold nanoparticle (Au NP) formation, with the supramolecular hydrogel being key to control and stabilize Au NPs, yielding a nanocomposite that catalyzed the photodegradation of a dye. Importantly, the Au NP formation occurred without the use of reductants other than the peptide, and the redox chemistry was investigated by LC-MS and NMR. This study provides important insights for the rational design of simple peptides as minimalistic and green building blocks for functional nanocomposites.

Peptides have long fascinated chemists for being widely used by nature as building blocks in both structural and functional roles.[1-2] Tripeptides are particularly interesting because they are simple enough to be made on a large scale by low-cost liquid-phase methods, while containing sufficient biochemical information to exert bioactivity.[3-4] Examples include Arg-Gly-Asp[5] and Leu-Asp-Val[6] that mediate cell adhesion, whereby Asp is key for function,[7] or Asp-Leu-Phe[8] that

inhibits bacterial replication, potentially useful to develop antibiotics. Asp was shown to be critical also for sweet-tasting dipeptides, *e.g.*, aspartame (Asp-Phe-OMe).[9] Strikingly, the non-proteinogenic D-Asp is an endogenous neurotransmitter[10-11] that was proposed to treat cognitive defects, as it stimulates myelin repair,[12] and affects testosterone levels.[13]

Short-peptide nanofibrils are convenient adjuvants for bioactive sequences.[14-16] However, design rules remain elusive for gelling di- and tri-peptides featuring Asp.[17-18] Seminal work by Reches and Gazit on Phe-Phe nanotubes enabled the search for other self-assembling sequences.[19] Hydrophobicity is a key driver of self-association in water, as demonstrated by a pioneering collaboration between Tuttle's and Ulijn's teams.[17] A successful approach thus includes using hydrophobic Phe-Phe, as in Asp-Phe-Phe and Phe-Phe-Asp that were studied as emulsifiers. They were predicted *in silico* to assemble into bilayers, although neither gels nor fibrils were observed at neutral pH.[20] Conversely, the more hydrophobic Fmoc-Phe-Phe-Asp assembled at pH 5-7 into nanofilaments.[21] Terminal modifications yielded gels from Ac-Phe-Leu-Asp-NH_2, Ac-Ile-Val-Asp, and related sequences,[22-23] but subtle structural changes often hamper hydrogelation for reasons that remain unknown.[24]

An alternative approach to design gelling di- and tri-peptides features heterochirality, *i.e.,* the inclusion of D- and L-residues at specific locations to direct the spatial positioning of side-chains within amphiphilic superstructures.[25] Heterochirality has enabled the design of supramolecular nanotubes,[26-27] gels,[28] 2D-sheets,[29] helical tapes[30] and fibrils.[31] In the case of Phe-Phe, heterochirality did not impact the backbone conformation or hydrogen-bonding pattern in the nanotubes, surprisingly.[32] However, it profoundly affected the orientation of Phe side-chains, leading to intra- instead of inter-molecular interactions that hindered hierarchical bundling into toxic microtubes, yielding instead biocompatible, gelling nanotubes.[32]

In light of the importance of hydrophilic residues such as Asp in bioactive motifs, here we analyzed the supramolecular behavior of the four stereoisomers of Phe-Phe-Asp (**Chart 1**), featuring a C-terminal Asp to promote intermolecular ionic interactions.[17] Single-crystal X-ray diffraction (XRD) structures of the four stereoisomers, as well as all-atom molecular dynamics (MDs), spectroscopic and microscopic analyses, provided a detailed picture, generating new understanding of the divergent behavior observed between stereoisomers upon application of a pH trigger. Surprisingly, subtle changes in stereoconfiguration stabilized conformers through intramolecular H-bonding, which in turn shifted pKa values to drive assembly to different outcomes. Furthermore, each peptide was tested for gold nanoparticle (NP) formation without adding further reductants, with only one stereoisomer yielding a hydrogel that enabled control over NP size and stability, yielding a nanocomposite that effectively catalyzed the photodegradation of a dye. Liquid-chromatography coupled to mass spectrometry (LC-MS), accurate MS, NMR, and infrared scattering-type near field optical microscopy (IR s-SNOM) analyses enabled the elucidation of the redox reaction.

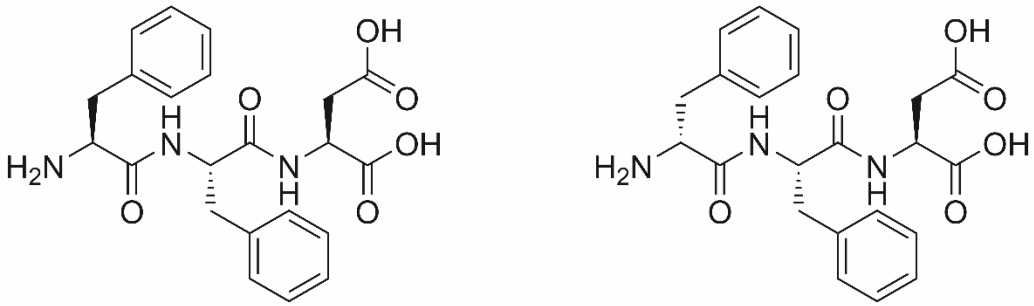

1 (L-L-L)

2 (D-L-L)

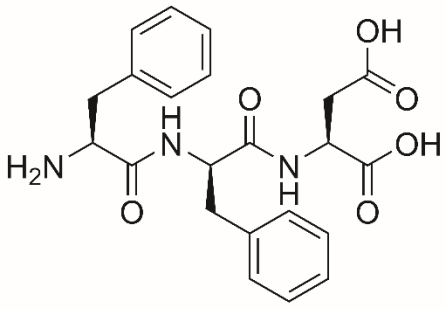

3 (L-D-L)

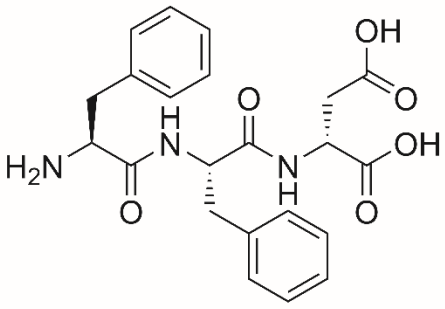

4 (L-L-D)

Chart 1. The four Phe-Phe-Asp stereoisomers.

Results and Discussion

Peptide self-assembly

There are eight stereoisomers of Phe-Phe-Asp: four enantiomeric pairs, which display identical supramolecular behavior in achiral environments. Compounds **1-4** (**Chart 1**) were prepared in solid-phase, HPLC-purified, and freeze-dried. They were fully characterized as described in ESI sections S1-S4. Self-assembly was triggered by switching from pH 12 to pH 5-6 using phosphate buffers. First, the anionic peptides were dissolved in phosphate buffer at alkaline pH thanks to intermolecular repulsion, then protonation of their N-termini at lower pH enabled the formation of intermolecular salt bridges (ESI section S5).[25] An acidic pH was required to protonate only one of

the two carboxylic groups, so that each zwitterionic molecule carried a neutral charge. The Asp side-chain pKa is known to be influenced by its position along a peptide sequence (pKa=5 was reported when C-terminal),[33] and its embedding in hydrophobic environments.[34]

Upon application of the pH trigger to **1-4**, only epimers **1** and **4** efficiently self-organized into hydrogels and crystals, respectively, whereas **2-3** yielded amorphous precipitates at concentrations above their solubility limit. The different macroscopic behavior of the four stereoisomers was rationalized in terms of each compound's ability to generate ordered amphiphilic superstructures, as confirmed by single-crystal XRD analyses (**Figure 1** and ESI section S5). All crystal structures show the presence of one deprotonated and one protonated COOH group, with similarity between the packing of **1** and **4**. In each a single peptide molecule is present in the asymmetric unit, with 3.5 or 1 solvent (water/methanol) molecules, respectively.

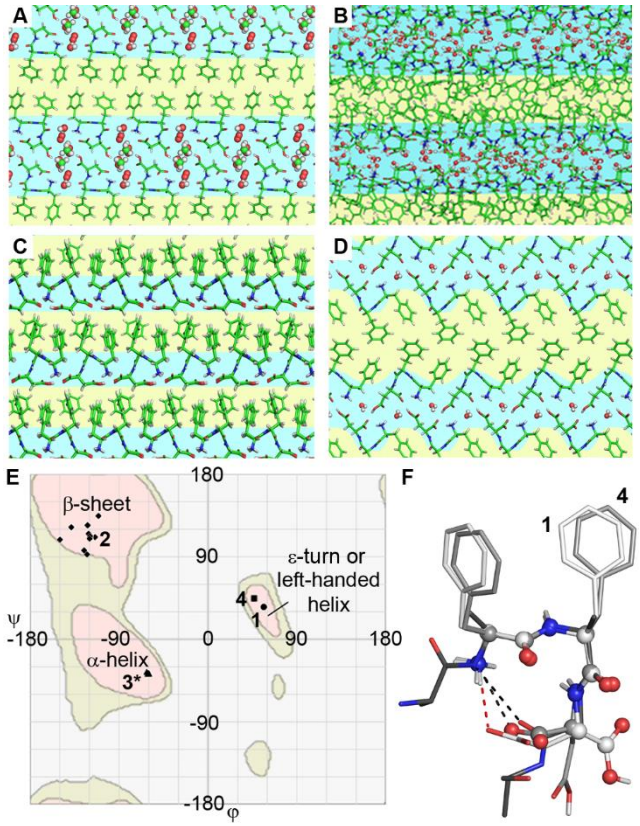

Figure 1. Single-crystal XRD structures of **1** (A), **2** (B), **3** (C), and **4** (D) show segregation of hydrophobic (yellow background) and hydrophilic (cyan background) moieties. Carbon atoms are shown in green, oxygen in red, nitrogen in blue, hydrogen in grey. E) Ramachandran plot of the dihedral angles of the central residue for **1-4**. Ten crystallographic independent molecules are shown for **2**. The inverted dihedral angles are reported for **3** as in this compound the central residue has a D-configuration (*denotes the enantiomer). F) Superimposition of the backbones of **1** (white) and **4** (light grey) with an ε-turn from PDB structure 2RA6 (dark grey).[35] Backbone atoms of all peptides are shown as spheres. Side chains of the 2RA6 structure have been removed for clarity.

In **4**, a strong intramolecular interaction is present, between the N- and C-termini. This backbone-to-backbone H-bond (NH(i)···CO(i+2)), which runs in opposite direction relative to α- (CO(i)···NH(i+4)), β- (CO(i)···NH(i+3)) and ϒ-turns (CO(i)···NH(i+2)), is a key feature of ε-turns.[36] This turn type, rare in proteins, is more common for cyclopeptides and heterochiral peptides. The backbone conformation of **4** is consistent with the family 4 of ε-turns (**Figure 1F**), which display Gly in position i+2, as recently reported by Toniolo *et al*.[35] Thus, the D-configuration of Asp in **4** appears crucial to form this ε-turn. The L-peptide **1** assumes an analogous conformation, however, a switch between the L-Asp terminal and side-chain carboxylates is necessary to retain the intramolecular interaction with the N-terminus (**Figure 1F**). In proteins, the side chain–main chain interaction is quite common for Asp. Over 16% of Asp is involved in the Asx-turns mimicking the β-turns.[37] However, the reverse direction of the H-bond observed in **1** is quite rare.[38]

Geometrical considerations on the chemical environment, supported by electron density maps, suggest the deprotonated state of the carboxylate involved in the intramolecular interaction in both **1** and **4**. The two epimers display different protonation states, with **4** being protonated on the Asp

side-chain (as in **3**), and **1** on the C-terminal COOH. The described intramolecular salt-bridge appears a key determinant of the peptide conformation and protonation state.

Conversely, the crystals of **2** and **3** displayed commensurately modulated structures (**Figure 1B-C**) with 10 and 3 peptide molecules in the asymmetric unit, respectively. The conformations of crystallographic independent molecules are similar for the backbone, but different for the side-chains (ESI section S5). Overall, we inferred that the higher order and efficient amphiphilic packing of **1** and **4** agreed with their effective self-assembly.

We investigated the tendency of **1** to gel, and **4** to crystallize, under the same conditions, through all-atom MD simulations. Similar conformers were adopted by **1** and **4**, although the acidic groups of the former engaged in intramolecular H-bonding to a greater extent than the latter (**Figure 2A-B** and ESI section S6). As a result, **1** displayed a higher pKa for the Asp side-chain COOH, as confirmed by *ab initio* quantum-mechanical calculations (ESI section S6), and experimentally by pH titrations (ESI section S7).

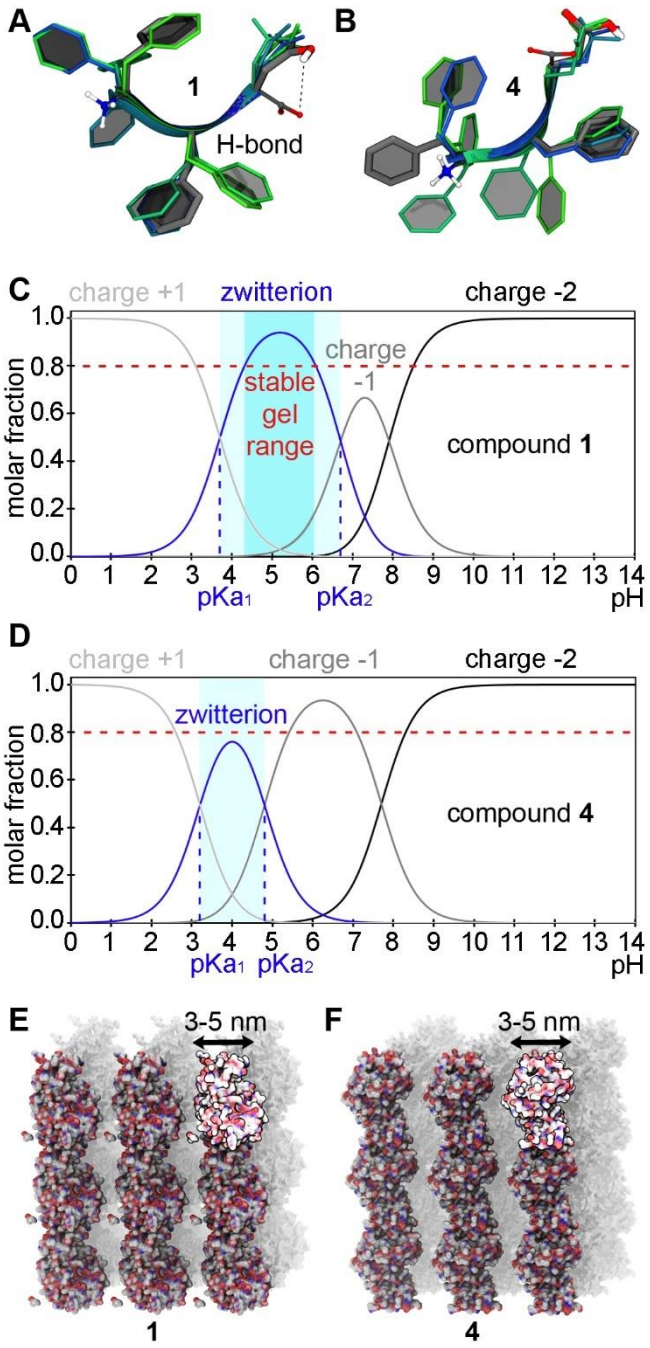

Figure 2. A-B) All-atom MDs in solution for **1** (A) and **4** (B). C-D) Speciation diagrams[39] for **1** (C) and **4** (D) at 20 mM revealed that only **1** was present as a zwitterion at ≥0.8 mole fraction (cyan) at pH 4-6, which gave stable gels. E-F) All-atom MDs of the zwitterions of **1** (E) and **4** (F) revealed nanofibrils, in agreement with TEM measurements. The molecular surfaces of peptide assemblies are shown, colored by atom type (C, N, and O in white, blue, and red, respectively).

The brightest surfaces identify the original simulation box. The solid dark colored and semi-transparent grey surfaces represent 8 and 18 additional boxes, respectively.

pKa shifts to higher values were noted for **1** as its concentration increased, especially for the Asp side-chain COOH (ESI section S7). This phenomenon was reported for self-assembling peptide derivatives, though never before linked to stereochemical effects, being ascribed to the non-covalent interactions and hydrophobic environment engendered during fibrillation.[40-43] **1** displayed the widest separation between the pKas of its two COOH groups, resulting in an optimal pH range of 4-6 at which the neutral zwitterion represented ≥0.8 of **1** mole fraction (**Figure 2C**, cyan area), yielding stable gels.

By contrast, **4** exhibited closer values for the pKas of the two COOH groups, thus never reaching 0.8 molar fraction of the neutral zwitterion at any given pH, and not undergoing gelation (**Figure 2D**). Further, the dipole moment for **4** (24.8 Db) was greater than for **1** (20.9 Db) in the crystal (ESI section S6). This observation, as well as the dipole orientation perpendicular to the peptide backbone, may explain the marked tendency of **4** to crystallize.[44]

All-atom MD simulation of both **1** and **4** confirmed their tendency to form fibrils (**Figure 2E-F** and ESI section S6) with diameters consistent with TEM measurements (**Figure 3** and ESI section S8). Analyses of the dihedral angles of the conformations sampled by **1** and **4** zwitterions during assembly, and of their ability to engage in H-bonding and salt bridges, did not reveal significant differences (ESI section S6). We inferred that gels were not observed for **4** because the neutral species never reached the critical threshold of 0.8 molar fraction (**Figure 2B**), in contrast to **1**, due to their differing pKas.

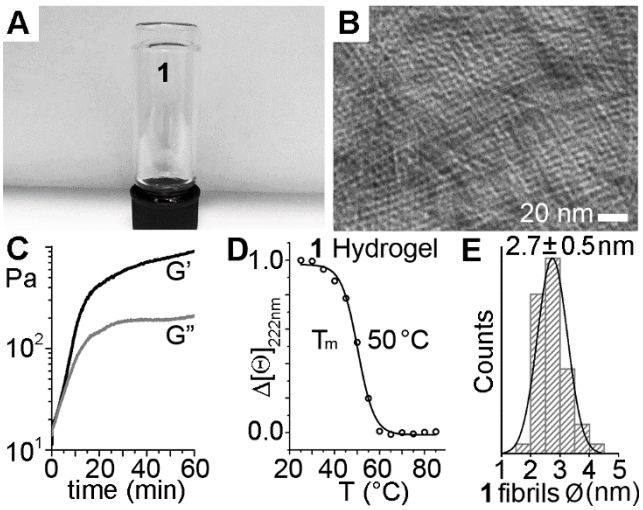

Figure 3. Nanostructured hydrogel **1**. A) Photograph of the gel. B) TEM micrograph reveals a nanofibrillar network. C) Gelation kinetics rheometry data. D) CD heating ramp reveals a T_m of 50 °C. E) Fibril diameter distribution (n = 150).

The nanostructured hydrogel of **1** (**Figure 3**) displayed an elastic modulus G' of 1 kPa after one hour of self-assembly, displaying a T_m of 50 °C. TEM analyses revealed homogenous fibrils with a diameter of 2.7 ± 0.5 nm (n = 150), in agreement with MDs (**Figure 2E**). Nanofibrils of analogous size were rarely observed for **2-4** (ESI, section S8), with **4** consistently crystallizing (**Figure 4A-B**). We inferred a general tendency for this sequence to fibrillate, as noted by MDs. CD spectra of **1-4** in solution (**Figure 4C**) were reminiscent of those assigned to a population of conformers featuring predominantly β-structures and turns.[25] The signs of the spectral features were dictated by the chirality of the central residue, hence negative at 200-240 nm for **3**, analogously to reports on stereoisomers of similar sequences.[45] At the higher concentrations needed for self-assembly, spectra could be acquired above 210 nm (**Figure 4D**). Significant differences were noted for **1** and **4**, with a sign inversion occurring, and overall signatures reminiscent of turns.

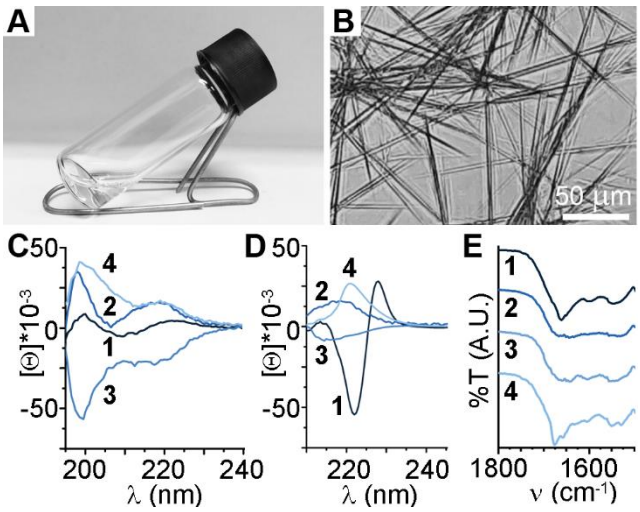

Figure 4. A) Gelation test for **4**. B) Microcrystals as seen by light microscopy. C-D) CD spectra of **1-4** in solution (C) and under self-assembly conditions (D). E) Amide region of the ATR-IR spectra of **1-4** under self-assembly conditions.

The amide region of Attenuated Total Reflectance infrared (ATR-IR) spectra under self-assembly conditions (**Figure 4E**) revealed broad signals for **2-3**, suggesting highly heterogeneous conformations. By contrast, sharper peaks arose for assembling **1** (1660, 1599, and 1536 cm^{-1}) and **4** (1674, 1660, 1599, and 1531 cm^{-1}), respectively, which fall in the regions of turns/left-handed helices.[35, 37] The absence of typical β-sheets formed by assembling peptides was confirmed by negligible fluorescence with the Thioflavin T amyloid stain (ESI section S11).[46]

Gold nanoparticle (Au NP) templating and size control

The four stereoisomers' assemblies were tested as templates for gold nanoparticles (Au NPs), using the peptide as reducing agent. Self-assembling peptides are widely used as supramolecular templates for Au NPs growth usually in the presence of a chemical reductant – unlike this work – and to our knowledge no studies thus far have investigated stereochemistry effects by selectively changing amino acid chirality from L- to D- within the peptide sequence.[47] In this work, we tested

the ability of the peptide to act as green reductant *in situ* for $HAuCl_4$, which was added to each peptide after self-assembly.

Interestingly, gold nanoparticles formed rapidly only within the homochiral **1** gel, which provided a supramolecular architecture that stabilized the NPs over time, impeding their aggregation. Conversely, over time, AuNPs formed also with the other stereoisomers, but with poor NP size and geometry control, and issues of aggregation (Figure 5A-B). The formation of NPs within the hydrogel of **1** displayed the typical rise of the absorbance peak at 538 nm (Figure 5C), corresponding to crystalline, polygonal, quasi-spherical NPs with an average diameter of 5.6 ± 2.6 nm (Figure 5D-E). The hydrogel nanocomposite successfully catalyzed the photodegradation of the organic dye methylene blue using a solar simulator (Figure 5F).

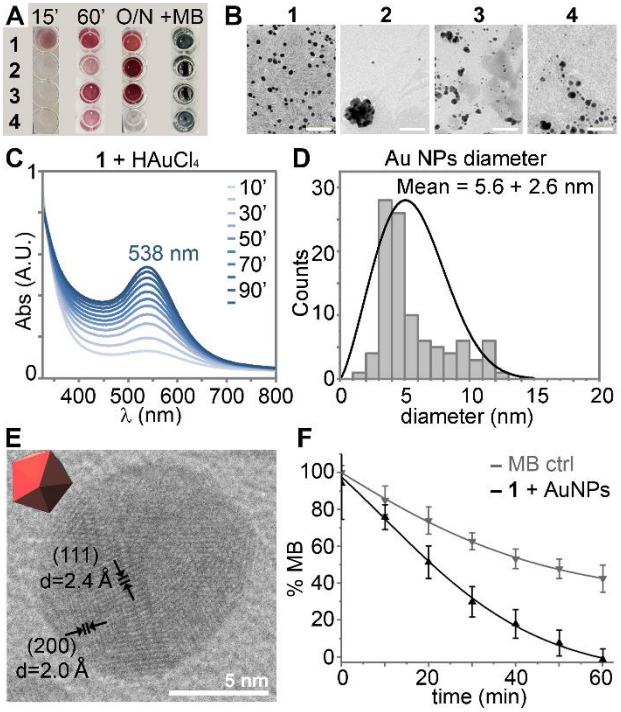

Figure 5. A) AuNPs form readily within the hydrogel of **1**, whose architecture provides stability against aggregation, contrarily to samples **2-4** (O/N = overnight; MB = methylene blue). B) Transmission electron microscopy (TEM) of AuNPs formed with peptides **1-4**, scalebar = 50 nm.

C) UV-absorbance of Au NPs formed within **1** hydrogel. D) Diameter distribution of Au NPs formed within **1** hydrogel (n = 100 counts). E) HR-TEM of Au NPs formed with **1**. F) Photocatalytic degradation of methylene blue (MB) in the presence of the composite hydrogel of **1** with Au NPs.

The conditions for NP formation were selected from a series of experiments that revealed that mild heating to 40 °C accelerated the process, yielding clusters of nanocrystallites during the first 30 minutes (Figure 6A-D), which then fused in polygonal nanoparticles over an hour (Figure 6E-G). However, heating the hydrogel immediately after $HAuCl_4$ addition, and/or using a peptide concentration >30 mM, resulted in inhomogeneous distribution of the NPs within the gel, with their consequent aggregation, and bigger NPs (16.2 ± 4.9 nm, n = 100), while peptide fibrils and their bundles were maintained (Figure 6F, 6H). Conversely, working at the minimum gel concentration (mgc) and incubating the gel with $HAuCl_4$ at room temperature for 30 minutes prior to heating, enabled the diffusion of the reagent within the gel, leading to a homogenous nanocomposite with good control over NP size, as shown in Figure 5.

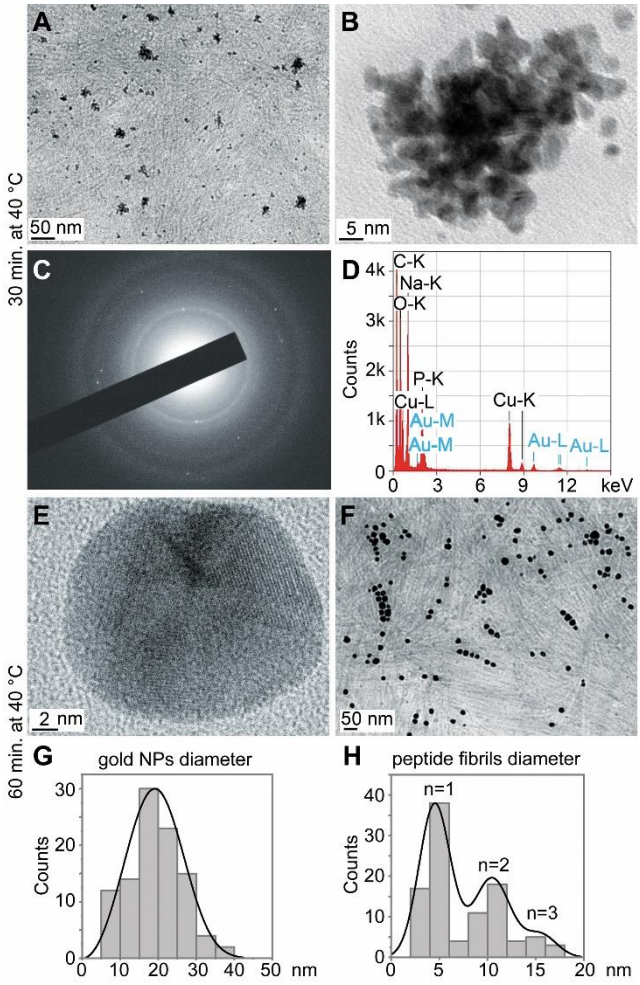

Figure 6. Study of AuNP formation within the hydrogel of **1** at 40 °C. A-D) During the first 30 minutes, polycrystalline NP clusters were found by TEM (A, B) and selected area electron diffraction, SAED (C), with energy-dispersive X-ray analysis (D) confirming presence of gold. E-H) Within an hour, the clusters merged into quasi-spherical NPs (E-G), dispersed in the hydrogel matrix (F), with peptide fibrils and their bundles present (H).

Furthermore, the reaction mixture was analyzed by LC-MS, HR-MS, and NMR (Figure 7A-C and ESI, Section S13), enabling identification of the unreacted peptide and two other species, one corresponding to the peptide-gold (III) complex, and another one corresponding to the oxidized peptide byproduct. The tetradentate coordination with gold (III) occurred in a classical mode (see

Figure 7A and ESI, Section S13), via the N-terminal neutral amine, two deprotonated amide nitrogen atoms, and one carboxylate, as already reported for other tripeptides devoid of coordinating groups in their sidechains.[48-50] Interestingly, in those cases the complexes were stable and could be isolated for structural elucidation, while gold reduction to Au(0) required the introduction of amino acids with gold-chelating, and oxidation-prone, functionalities on the sidechain, *i.e.*, Tyr[51] or Cys.[52] We attributed the difference in reactivity to the presence of Asp, whose oxidized dehydroderivative (ΔAsp) can undergo Michael additions more promptly than Phe,[53-54] thus driving the redox reaction towards product formation. Indeed, the oxidized tripeptide byproduct displayed a mass corresponding to ΔPhe-ΔPhe-ΔAsp added with water (see ESI, Section S13). The product was further confirmed by accurate MS of the sample prepared in deuterated water, which yielded the corresponding deuterated product with the expected increase in mass (see ESI, Section S14). Furthermore, full-atom molecular models of the Au(III) complex of the four stereoisomers (Figure 7D) did not reveal any significant structural and energetic difference between them. We inferred that the amino acid nature is key in the redox process, as opposed to the stereoconfiguration, in agreement with the observed formation of Au NPs in the presence of any peptide **1-4**. Conversely, chirality effects determine the peptides' self-assembly macroscopic outcome, thus their ability to stabilize Au NPs within a supramolecular gel architecture against their aggregation.

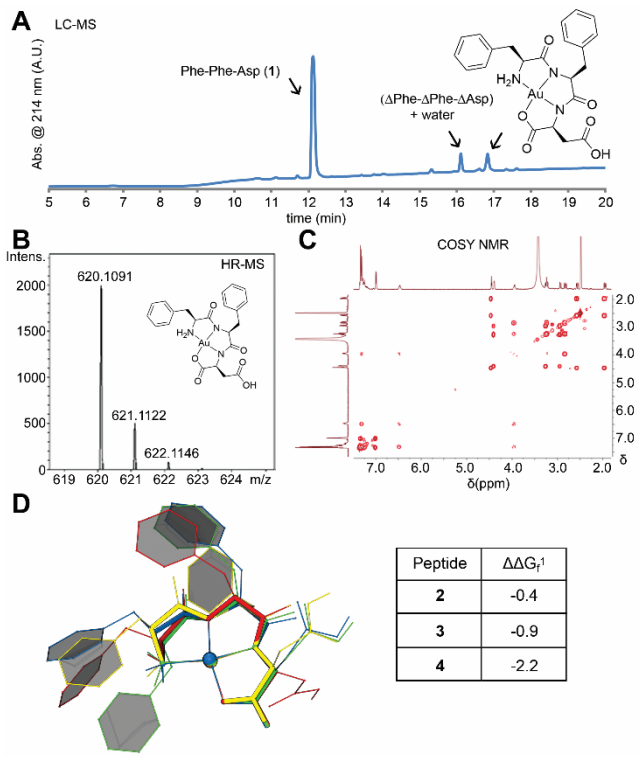

Peptide	$\Delta\Delta G_f^1$
2	-0.4
3	-0.9
4	-2.2

Figure 7. A) LC-MS chromatographic trace of the reaction mixture. B) HR-MS spectrum and C) gCOSY NMR spectrum of the isolated Au(III)-peptide **1** complex. D) Structural differences between the Au(III) complexes with peptide **1** (light blue), **2** (green), **3** (yellow), and **4** (red). Atoms of the backbone (including the COO terminus) are shown by thicker sticks to highlight the structural similarity of the complexes. The inset table shows differences in the free energies of formation (kcal/mol) of peptides **2-4** relative to **1**. See ESI Section S6 for methodological details.

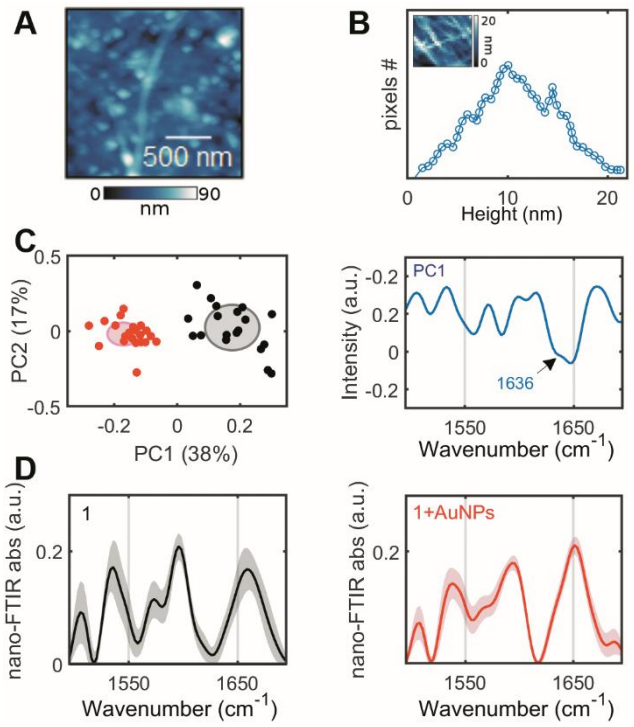

Figure 8. A) AFM topography map of **1** nanocomposite with AuNPs. B) Height distribution of **1** with AuNPs calculated on a representative region of isolated fibrils (with topography shown in the inset). C) PCA scores (left) and PC1 loading (right, accounting for 38% of the variance) on **1** (black) and **1** nanocomposite with AuNPs (red). D) IR s-SNOM average spectra of **1** (black) and **1** nanocomposite with AuNPs (red), with standard deviation shown as a shadow.

Finally, we exploited infrared scattering-type scanning near field optical microscopy (IR s-SNOM)[55] on the supramolecular gel of **1** without and with AuNPs (Figure 8) with the aim to link the composite nanomorphology with its chemistry. Atomic force microscopy (AFM) imaging of the gel nanocomposite of **1** with AuNPs (Figure 8A) confirmed the expected fibrillar nanomorphology with a fibril height distribution (Figure 8B) matching the fibril width observed by TEM (Figure 6H). TEM results were also confirmed for sample **1** (See ESI Section 13, Fig S59).

Principal component analysis (PCA) of the infrared spectral data revealed a clear separation of the two samples along the principal component 1, PC1(Figure 8C, left panel), that accounted for 38% of the total variance of the system. PC1 loading (Figure 8C, right panel) showed that the discrimination was mostly driven by the spectral components centered at 1648 cm^{-1} and 1636 cm^{-1}, these moieties being more prominent in the nanocomposite. This information could be also drawn out by comparing the average spectra of **1** gel without and with AuNPs, shown in Figure 8D, left and right panel respectively. Point spectra for a selected region of each sample were reported and correlated to the sample morphology at ESI, Section S13 Fig. S60. The peak centered at 1651 cm^{-1} (1648 cm^{-1} in PC1 loading) for the nanocomposite, and at 1660 cm^{-1} for sample **1** without AuNPs, could be associated to the peptide backbone amide I vibration. Since this mode is strongly affected by transition dipole coupling between adjacent peptide bonds, the difference observed in the amide I spectral position reflected differences in the backbone arrangement in the two samples. In addition, the prominence of the peak centered at 1636 cm^{-1} in the nanocomposite supported the formation of the dehydropeptide byproduct, since it could be ascribed to the C_α=C_β stretching vibration frequency, as reported for ΔPhe.[56] The ATR-IR spectra for the gel of **1** without and with AuNPs (Fig. S61, in ESI Section S13) revealed signals for the latter in agreement with the nano-resolved IR spectra.

Conclusions

This work unraveled the fine details that lead four peptide stereoisomers towards different macroscopic outcomes as a result of self-assembly, and how they can be applied to template Au NP formation. The tripeptides were synthesized, purified, and characterized by LC-MS, ^{1}H- and ^{13}C-NMR. Single-crystal XRD analysis using synchrotron radiation revealed a higher

supramolecular order for **1** and **4**, both of which adopt a rare turn conformation that was supported by circular dichroism and infrared spectroscopy. Both **1** and **4** tend to fibrillate, as shown by TEM micrographs and all-atom MD studies, while testing negative to amyloid staining for β-sheets. Interestingly, experimental pKa titrations and *ab initio* quantum-mechanical calculations showed how **1** engages in intramolecular H-bonding in solution that shifts its acidic pKa to enable sufficient formation of the zwitterionic species that gels at mildly acidic pH, contrarily to the other stereoisomer.

All four tripeptides could be used as mild reducing agents to convert Au(III) to AuNPs, through the generation of structurally and energetically similar tetradentate gold complexes. The reaction could further proceed to yield the oxidized dehydropeptides that underwent Michael addition of water on the Asp residue, as confirmed by several spectroscopy techniques and a control experiment with deuterated water. However, the presence of a supramolecular gel architecture for **1** proved key to control the growth of Au NPs and avoid their aggregation. The resulting nanocomposite was successfully used for the photocatalytic degradation of a dye using a solar simulator.

In conclusion, this work allows extension of self-assembly rules for heterochiral minimalistic peptides[25] to sequences with hydrophilic side-chains, as often found in bioactive motifs. Understanding regarding to how to modulate the pKa values of ionizable groups may enable the design of self-assembling short motifs into bioactive hydrogels.[5-13] Furthermore, we studied stereochemical effects on gold NP formation and stabilization in a nanocomposite, and provided insights into the redox reaction mechanism and products with aspartic acid playing an elected role. Amino acids and their amphiphilic derivatives are raising considerable interest for the templation of gold chiral nanostructures, with elegant examples exploiting cysteine as ligand being reported

by Nam's[57] and Liz-Marzan's[58] groups. Therefore, the knowledge gathered in this work could potentially expand the amino acid toolbox in the supramolecular templation of gold nanostructures via self-assembly.

We anticipate biological applications, whereby subtle pH differences between pathological and physiological states can be a convenient trigger to selectively achieve fibrillation, *e.g.*, in the acidic environment of cancer cells.[59-61] The ability to attain fine control over peptide self-organization opens new horizons in theranostics, and to direct cell fate.[62-67] Further work will address applications of these materials, to unlock their potential to interfere with biological systems in useful ways.

Materials and Methods

Peptide synthesis, purification, and molecular spectroscopic characterization. All chemicals (analytical grade) were acquired from Merck. Compounds **1-4** were obtained by solid-phase synthesis using standard protocols.[68] The products were purified using HPLC (Agilent 1260 Infinity system) with a C-18 column (Kinetex, 5 microns, 100 Å, 250 x 10 mm, Phenomenex) and a gradient of acetonitrile (MeCN) / water with 0.05% TFA as follows: t = 0- 2 min. 30% MeCN; t = 10 min. 70% MeCN; t = 12-15 min. 95% MeCN (R_t= 10-12 min). Fractions with the pure products were lyophilized and characterized by Electron Ionisation-Mass Spectroscopy (ESI-MS) and by Nuclear Magnetic Resonance Spectroscopy (^{1}H-NMR and ^{13}C-NMR). Spectra are provided in the ESI Sections S1-S4. In particular, the ESI-MS analyses were performed on samples dissolved in mixture 50:50 H_2O/MeCN with 0.1% of Formic Acid (FA), using an analytical C-18 column (Luna, 5 µm, 100 Å, 150 x 2 mm, Phenomenex) and Quadrupole LC-MS (6120). The ^{1}H-NMR and ^{13}C-NMR spectra were recorded in Dimethyl sulfoxide (DMSO-*d6*), using

tetramethylsilane (TMS) as internal standard, with a *Varian Innova* spectrometer at the frequency of 400 and 100 MHz, respectively. General methods are described in the ESI.

Self-Assembly Protocol. Each peptide was dissolved at 70 mM in 0.1 M sodium phosphate at pH 11.8. Subsequent dilution with an equal volume of 0.2 M sodium phosphate at pH 4.5 led to samples with a final concentration of 35 mM and a pH of 5.9 and 0.15 M sodium phosphate. Compound **1** formed self-supporting hydrogels, which formed also in deionized water (at concentrations ≥ 20 mM, and final pH values 4.5-5.5), or with 0.1M sodium phosphate (at final pH values 4.5-5.8). Compounds **2-3** led to clear solutions, and at higher concentrations (40-45 mM) amorphous precipitates were formed. Compound **4** formed microcrystals (35-40 mM).

Crystallization. Compound **4** crystallized within minutes using the self-assembly protocol described above. Single crystals of peptides **1-3** were grown by vapor diffusion by dissolving **1-3** at 2 mM in 2 mL of MeOH inside a reservoir with 3 mL of a mixture of methanol/water (80:20). The peptides crystallized over a month. Crystallographic details are provided in ESI Section S5.

Gold complex synthesis and purification. Peptide **1** was dissolved at 60 mM in 0.1 sodium phosphate at pH 11.8. The subsequent dilution with an equal volume of 0.2 M sodium phosphate at pH 4.5 led to sample solution with final concentration of 30 mM at pH 6.00. A stock solution of $AuCl_4^-$ at 294.3 mM was added to peptide solution reaching a final concentration of 25 mM. The yellow solution was stirred at 40 °C overnight, after 1 h the solution turned to purple because of the AuNPs formation. The crude was centrifuged to remove the nanoparticles and the supernatant freeze-dried. The powder was dissolved in a solution 20:80 MeCN:H_2O and purified through reverse phase HPLC on an Agilent 1260 Infinity system equipped with a gradient pump, C-18 column (Kinetex, 5 microns, 100 Å, 250 x 10 mm, Phenomenex), autosampler, and photodiode array detector. The gradient consisted of MeCN / H_2O with 0.05% TFA as follows: t

= 0- 2 min. 20% MeCN; t = 38 min. 95% MeCN; t = 40 min. 95% MeCN (Rt= 13.95-14.50 min). The product was freeze-dried and characterized by Electron Ionisation-Mass Spectroscopy (ESI-MS) and by Nuclear Magnetic Resonance Spectroscopy (^{1}H-NMR and ^{13}C-NMR). Spectra are provided in the ESI Section S13. In particular, the accurate mass analysis was performed on sample dissolved in mixture 5:47.5:47.5 DMSO:H_2O:MeCN with 0.1% of FA, using a Bruker micrOTOF-Q with ESI source. For the acquisition the instrument was set as follows: scan begin 50 m/z, scan end 1500 m/z, ion polarity Negative, set Capillary 3200 V, set Nebulizer 0.4 Bar, set Dry Heater 200 °C, set Dry Gas 4.0 l/min. The ^{1}H-NMR and ^{13}C-NMR spectra were recorded in Dimethyl sulfoxide (DMSO-d6), using tetramethylsilane (TMS) as internal standard, with a Varian Innova spectrometer at the frequency of 500 and 125 MHz.

Nanocomposite formation in deuterated water. Peptide **1** was dissolved in D_2O at concentration 30 mM and the pH was adjusted to 5.8, to trigger the gel formation, with a solution of NaOD 20 wt%. After 1 hour a stock solution of $AuCl_4^-$ (294.3 mM) was added to the gel in order to have a final ratio peptide:gold of 10:1. The samples was heated at 40°C for 1 hour and the AuNPs formation was confirmed by the purple color of the gel. (ESI Section S14, Figure S63).

Generation of tripeptide structural models. Models of zwitterionic tripeptides **1** and **4** were built upon the experimental structures. The sidechain of the C-terminal L/D aspartic acid was protonated on one of the two oxygens. All other hydrogens were added by loading the 3D structures into the *tleap* module of the AMBER20 package,[69] which was also used to perform all MD simulations.

MD simulations. For each tripeptide, we performed one MD simulation of a single molecule in water and multi-copy (three) MD simulations of the self-assembly process for 216 tripeptides.

Simulations were performed following the protocol described previously.[25] Further details can be found in the ESI section S6.

Gold complexes *in silico* studies. Structural models and formation free energies of all tripeptides in complex with Au(III) were estimated using Gaussian16 in the presence of implicit solvent. Further details can be found in the ESI section S6.

Gold NP templating. 100-μL samples of peptides **1-4** were prepared at 30 mM according to the self-assembly protocol described above in triplicates of 96-well plates. After 1 hour, 1.02 μL of an aqueous solution of $HAuCl_4$ (300 mM) was gently added on top, and samples were incubated first at room temperature for 30 min., then at 40 °C for various times as indicated in the text.

Methylene Blue Dye Degradation. Nanocomposites with gold NPs were prepared as described above using a final incubation at 40 °C for 90 minutes to complete the process of NP formation. The, 10 μL of an aqueous solution of methylene blue dye (0.5 mM) were added on top to reach a final concentration of 0.05 mM, and samples were transferred inside a Lot-Oriel Solar Simulator equipped with a 150 W Xe lamp and an Atmospheric Edge Filter with a cut-off at 300 nm, with irradiation for 1 hour. Readings at 664 nm were carried out at various timepoints inside a Tecan Infinite Pro Plus.

Infrared nanoscopy. Infrared analysis at the nanoscale was performed at the SISSI-Bio (Synchrotron Infrared Source for Spectroscopy and Imaging, life science branch) beamline of Elettra Sincrotrone Trieste thanks to the use of a IR s-SNOM (IR scattering-type scanning near field optical microscopy) instrument (Attocube Systems AG, Munich GE),[70] coupled with a DFG (Difference Frequency Generation) laser operating in the region between 1300-1900 cm^{-1}. Samples were prepared as describe din the above sections, dropped on a clean silicon wafer substrate and dried overnight *in vacuo*. A conductive tip (Neaspec) was used, with nominal tip radius of 20 nm working at a tapping frequency of 240 kHz. A tapping amplitude of 100 nm was exploited for spectroscopy measurements that were acquired a 7 cm^{-1} spectral resolution by accumulating 5 interferometric scans. Sample spectra were referenced with the spectrum acquired on clean silicon substrate. 2^{nd}-harmonic of the imaginary part of the signal was used as representative of nano-FTIR absorption, according to published procedures.[55, 71] The experimental setup allowed to acquire topographic maps with lateral resolution of 20 nm, comparable with the tip radius, and punctual infrared spectra on sample surfaces of the lateral resolution. A random sampling on fibers in dry samples were performed by acquiring a minimum of 20 spectra per sample. Principal Component Analysis (PCA) was performed (Quasar 1.7.0) with the aim to discriminate key features occurring in the spectra of the nanocomposite, compared with sample **1** as control.[72] Spectra were first cut (1495-1700 cm^{-1}) and baseline corrected (positive rubber-band filter). A vector normalization was then applied to eliminate possible data separations due to differences in sample thickness. Last, a Savitsky-Golay filter, with 17 smoothing points was applied prior to PCA processing. Average spectra were calculated by following the same processing employed for PCA analysis, but no smoothing filters were applied on spectra.

ASSOCIATED CONTENT

Supporting Information. Spectroscopic characterization of the four peptides, self-assembly method, crystallographic details, in silico studies, pH titrations, TEM images, rheological data, infrared spectra, CD spectra, fluorescence data, characterization of the gold complex and redox reaction (PDF), crystallographic structures (cif files).

AUTHOR INFORMATION

Corresponding Author

*vargiu@dsf.unica.it *rdezorzi@units.it *smarchesan@units.it

Author Contributions

The manuscript was written through contributions of all authors. All authors have given approval to the final version of the manuscript.

ACKNOWLEDGMENT

The authors are grateful to Professor Peter Comba (University of Heidelberg) for useful scientific discussions. The authors acknowledge funding from the Italian Ministry of University and Research (MIUR) SIR grant n. RBSI14A7PL to S.M., the Royal Society of Chemistry (UK) Research Fund n. R21-7388144754 to S.M., The University of Trieste for the grant FRA2023 to S.M., the Slovenian Research Agency (ARIS: P2-0089, J2-3043, J2-3040, J2-3046, J3-3079, J7-4420 and bilateral ARIS projects BI-FR/23-24-PROTEUS-005 and BI-RS/23-25-030 to S.K.), and the CENN Nanocenter for TEM access. Elettra Sincrotrone Trieste is acknowledged for access to its synchrotron radiation facilities, and M. Polentarutti for assistance on the XRD1 beamline. This research used the Savio computational cluster resource provided by the Berkeley Research Computing program at the University of California, Berkeley. We are thankful to Fabio Hollan (University of Trieste) for technical assistance with mass spectrometry.

ABBREVIATIONS

LC-MS, liquid chromatography – mass spectrometry; NMR, nuclear magnetic resonance; PDB, protein databank; XRD, X-ray diffraction.

REFERENCES

1. Amit, M.; Yuran, S.; Gazit, E.; Reches, M.; Ashkenasy, N., Tailor-Made Functional Peptide Self-Assembling Nanostructures. *Adv. Mater.* **2018,** *30* (41), 1707083.
2. Lampel, A., Biology-Inspired Supramolecular Peptide Systems. *Chem* **2020,** *6* (6), 1222-1236.
3. Ung, P.; Winkler, D. A., Tripeptide Motifs in Biology: Targets for Peptidomimetic Design. *J. Med. Chem.* **2011,** *54* (5), 1111-1125.
4. Marin, D.; Marchesan, S., Self-Assembled Peptide Nanostructures for ECM Biomimicry. **2022,** *12* (13), 2147.
5. Ruoslahti, E.; Pierschbacher, M. D., New perspectives in cell adhesion: RGD and integrins. *Science* **1987,** *238* (4826), 491-7.
6. Komoriya, A.; Green, L. J.; Mervic, M.; Yamada, S. S.; Yamada, K. M.; Humphries, M. J., The minimal essential sequence for a major cell type-specific adhesion site (CS1) within the alternatively spliced type III connecting segment domain of fibronectin is leucine-aspartic acid-valine. *J. Biol. Chem.* **1991,** *266* (23), 15075-9.
7. Liyanage, W.; Vats, K.; Rajbhandary, A.; Benoit, D. S. W.; Nilsson, B. L., Multicomponent dipeptide hydrogels as extracellular matrix-mimetic scaffolds for cell culture applications. *Chem. Commun.* **2015,** *51* (56), 11260-11263.
8. Wijffels, G.; Johnson, W. M.; Oakley, A. J.; Turner, K.; Epa, V. C.; Briscoe, S. J.; Polley, M.; Liepa, A. J.; Hofmann, A.; Buchardt, J.; Christensen, C.; Prosselkov, P.; Dalrymple, B. P.; Alewood, P. F.; Jennings, P. A.; Dixon, N. E.; Winkler, D. A., Binding Inhibitors of the Bacterial Sliding Clamp by Design. *J. Med. Chem.* **2011,** *54* (13), 4831-4838.
9. Mazur, R. H.; Schlatter, J. M.; Goldkamp, A. H., Structure-taste relationships of some dipeptides. *J. Am. Chem. Soc.* **1969,** *91* (10), 2684-2691.
10. D'Aniello, S.; Somorjai, I.; Garcia-Fernàndez, J.; Topo, E.; D'Aniello, A., D-Aspartic acid is a novel endogenous neurotransmitter. *FASEB J.* **2011,** *25* (3), 1014-1027.
11. Errico, F.; Cuomo, M.; Canu, N.; Caputo, V.; Usiello, A., New insights on the influence of free d-aspartate metabolism in the mammalian brain during prenatal and postnatal life. *Biochim. Biophys. Acta Proteins Proteom.* **2020,** *1868* (10), 140471.
12. de Rosa, V.; Secondo, A.; Pannaccione, A.; Ciccone, R.; Formisano, L.; Guida, N.; Crispino, R.; Fico, A.; Polishchuk, R.; D'Aniello, A.; Annunziato, L.; Boscia, F., D-Aspartate treatment attenuates myelin damage and stimulates myelin repair. *EMBO Mol. Med.* **2019,** *11* (1), e9278.
13. Roshanzamir, F.; Safavi, S. M., The putative effects of D-Aspartic acid on blood testosterone levels: A systematic review. *Int. J. Reprod. Biomed.* **2017,** *15* (1), 1-10.
14. Spicer, C. D.; Jumeaux, C.; Gupta, B.; Stevens, M. M., Peptide and protein nanoparticle conjugates: versatile platforms for biomedical applications. *Chem. Soc. Rev.* **2018,** *47* (10), 3574-3620.
15. Schnaider, L.; Ghosh, M.; Bychenko, D.; Grigoriants, I.; Ya'ari, S.; Shalev Antsel, T.; Matalon, S.; Sarig, R.; Brosh, T.; Pilo, R.; Gazit, E.; Adler-Abramovich, L., Enhanced

Nanoassembly-Incorporated Antibacterial Composite Materials. *ACS Appl. Mater. Interfaces* **2019,** *11* (24), 21334-21342.
16. Contreras-Montoya, R.; Arredondo-Amador, M.; Escolano-Casado, G.; Mañas-Torres, M. C.; González, M.; Conejero-Muriel, M.; Bhatia, V.; Díaz-Mochón, J. J.; Martínez-Augustin, O.; de Medina, F. S.; Lopez-Lopez, M. T.; Conejero-Lara, F.; Gavira, J. A.; de Cienfuegos, L. Á., Insulin Crystals Grown in Short-Peptide Supramolecular Hydrogels Show Enhanced Thermal Stability and Slower Release Profile. *ACS Appl. Mater. Interfaces* **2021,** *13* (10), 11672-11682.
17. Frederix, P. W.; Scott, G. G.; Abul-Haija, Y. M.; Kalafatovic, D.; Pappas, C. G.; Javid, N.; Hunt, N. T.; Ulijn, R. V.; Tuttle, T., Exploring the sequence space for (tri-)peptide self-assembly to design and discover new hydrogels. *Nat. Chem.* **2015,** *7* (1), 30-37.
18. Frederix, P. W. J. M.; Ulijn, R. V.; Hunt, N. T.; Tuttle, T., Virtual Screening for Dipeptide Aggregation: Toward Predictive Tools for Peptide Self-Assembly. *J. Phys. Chem. Lett.* **2011,** *2* (19), 2380-2384.
19. Reches, M.; Gazit, E., Casting metal nanowires within discrete self-assembled peptide nanotubes. *Science* **2003,** *300* (5619), 625-627.
20. Scott, G. G.; McKnight, P. J.; Tuttle, T.; Ulijn, R. V., Tripeptide Emulsifiers. *Adv. Mater.* **2016,** *28* (7), 1381-1386.
21. Li, Q.; Zhang, J.; Wang, Y.; Qi, W.; Su, R.; He, Z., Peptide Templated Synthesis of TiO_2 Nanofibers with Tunable Photocatalytic Activity. *Chem. Eur. J.* **2018,** *24* (68), 18123-18129.
22. Sahoo, J. K.; Nazareth, C.; VandenBerg, M. A.; Webber, M. J., Self-assembly of amphiphilic tripeptides with sequence-dependent nanostructure. *Biomater. Sci.* **2017,** *5* (8), 1526-1530.
23. Sahoo, J. K.; Nazareth, C.; VandenBerg, M. A.; Webber, M. J., Aromatic identity, electronic substitution, and sequence in amphiphilic tripeptide self-assembly. *Soft Matter* **2018,** *14* (45), 9168-9174.
24. Chan, K. H.; Xue, B.; Robinson, R. C.; Hauser, C. A. E., Systematic Moiety Variations of Ultrashort Peptides Produce Profound Effects on Self-Assembly, Nanostructure Formation, Hydrogelation, and Phase Transition. *Sci. Rep.* **2017,** *7* (1), 12897.
25. Garcia, A. M.; Iglesias, D.; Parisi, E.; Styan, K. E.; Waddington, L. J.; Deganutti, C.; De Zorzi, R.; Grassi, M.; Melchionna, M.; Vargiu, A. V.; Marchesan, S., Chirality Effects on Peptide Self-Assembly Unraveled from Molecules to Materials. *Chem* **2018,** *4* (8), 1862-1876.
26. Chapman, R.; Danial, M.; Koh, M. L.; Jolliffe, K. A.; Perrier, S., Design and properties of functional nanotubes from the self-assembly of cyclic peptide templates. *Chem. Soc. Rev.* **2012,** *41* (18), 6023-6041.
27. Brendel, J. C.; Sanchis, J.; Catrouillet, S.; Czuba, E.; Chen, M. Z.; Long, B. M.; Nowell, C.; Johnston, A.; Jolliffe, K. A.; Perrier, S., Secondary Self-Assembly of Supramolecular Nanotubes into Tubisomes and Their Activity on Cells. *Angew. Chem. Int. Ed.* **2018,** *57* (51), 16678-16682.
28. Méndez-Ardoy, A.; Granja, J. R.; Montenegro, J., pH-Triggered self-assembly and hydrogelation of cyclic peptide nanotubes confined in water micro-droplets. *Nanoscale Horiz.* **2018,** *3* (4), 391-396.
29. Insua, I.; Montenegro, J., 1D to 2D Self Assembly of Cyclic Peptides. *J. Am. Chem. Soc.* **2020,** *142* (1), 300-307.
30. Clover, T. M.; O'Neill, C. L.; Appavu, R.; Lokhande, G.; Gaharwar, A. K.; Posey, A. E.; White, M. A.; Rudra, J. S., Self-Assembly of Block Heterochiral Peptides into Helical Tapes. *J. Am. Chem. Soc.* **2020,** *142* (47), 19809-19813.

31. Wang, M.; Zhou, P.; Wang, J.; Zhao, Y.; Ma, H.; Lu, J. R.; Xu, H., Left or Right: How Does Amino Acid Chirality Affect the Handedness of Nanostructures Self-Assembled from Short Amphiphilic Peptides? *J. Am. Chem. Soc.* **2017,** *139* (11), 4185-4194.
32. Kralj, S.; Bellotto, O.; Parisi, E.; Garcia, A. M.; Iglesias, D.; Semeraro, S.; Deganutti, C.; D'Andrea, P.; Vargiu, A. V.; Geremia, S.; De Zorzi, R.; Marchesan, S., Heterochirality and Halogenation Control Phe-Phe Hierarchical Assembly. *ACS Nano* **2020**, *14* (12), 16951-16961.
33. Hinterholzer, A.; Stanojlovic, V.; Regl, C.; Huber, C. G.; Cabrele, C.; Schubert, M., Detecting aspartate isomerization and backbone cleavage after aspartate in intact proteins by NMR spectroscopy. *J. Biomol. NMR* **2021**, *75*, 71-82.
34. Silverstein, T. P., How enzymes harness highly unfavorable proton transfer reactions. *Protein Sci.* **2021**, *30* (4), 735-744.
35. Toniolo, C.; Crisma, M.; Formaggio, F.; Alemán, C.; Ramakrishnan, C.; Kalmankar, N.; Balaram, P., Intramolecular backbone···backbone hydrogen bonds in polypeptide conformations. The other way around: ε-turn. *Pept. Sci.* **2017,** *108* (1), e22911.
36. de Brevern, A. G., Extension of the classical classification of β-turns. *Sci. Rep.* **2016,** *6* (1), 33191.
37. Duddy, W. J.; Nissink, J. W.; Allen, F. H.; Milner-White, E. J., Mimicry by asx- and ST-turns of the four main types of beta-turn in proteins. *Protein Sci.* **2004,** *13* (11), 3051-5.
38. Vijayakumar, M.; Qian, H.; Zhou, H.-X., Hydrogen bonds between short polar side chains and peptide backbone: Prevalence in proteins and effects on helix-forming propensities. *Proteins: Struct. Funct. Bioinf.* **1999,** *34* (4), 497-507.
39. Gutz, I. G. R. *CurTiPot,* http://www.iq.usp.br/gutz/Curtipot_.html.
40. Tang, C.; Smith, A. M.; Collins, R. F.; Ulijn, R. V.; Saiani, A., Fmoc-diphenylalanine self-assembly mechanism induces apparent pKa shifts. *Langmuir* **2009,** *25* (16), 9447-53.
41. Cross, E. R.; Adams, D. J., Probing the self-assembled structures and pKa of hydrogels using electrochemical methods. *Soft Matter* **2019,** *15* (7), 1522-1528.
42. Tena-Solsona, M.; Nanda, J.; Díaz-Oltra, S.; Chotera, A.; Ashkenasy, G.; Escuder, B., Emergent Catalytic Behavior of Self-Assembled Low Molecular Weight Peptide-Based Aggregates and Hydrogels. *Chem. Eur. J.* **2016,** *22* (19), 6687-6694.
43. Garcia, A. M.; Lavendomme, R.; Kralj, S.; Kurbasic, M.; Bellotto, O.; Cringoli, M. C.; Semeraro, S.; Bandiera, A.; De Zorzi, R.; Marchesan, S., Self-Assembly of an Amino Acid Derivative into an Antimicrobial Hydrogel Biomaterial. *Chem. Eur. J.* **2020,** *26* (8), 1880-1886.
44. Koperwas, K.; Adrjanowicz, K.; Grzybowski, A.; Paluch, M., The role of the dipole moment orientations in the crystallization tendency of the van der Waals liquids – molecular dynamics simulations. *Sci. Rep.* **2020,** *10* (1), 283.
45. Marchesan, S.; Easton, C. D.; Styan, K. E.; Waddington, L. J.; Kushkaki, F.; Goodall, L.; McLean, K. M.; Forsythe, J. S.; Hartley, P. G., Chirality effects at each amino acid position on tripeptide self-assembly into hydrogel biomaterials. *Nanoscale* **2014,** *6* (10), 5172-5180.
46. Amdursky, N.; Erez, Y.; Huppert, D., Molecular rotors: what lies behind the high sensitivity of the thioflavin-T fluorescent marker. *Acc. Chem. Res.* **2012,** *45* (9), 1548-1557.
47. Bellotto, O.; Cringoli, M. C.; Perathoner, S.; Fornasiero, P.; Marchesan, S., Peptide Gelators to Template Inorganic Nanoparticle Formation. *Gels* **2021,** *7* (1), 14.

48. Koleva, B. B.; Kolev, T.; Lamshöft, M.; Spiteller, M., Synthesis, spectroscopic analysis and structure deduction of gold(III), palladium(II) and platinum(II) complexes with the tripeptide glycyl-l-phenylalanyl-glycine. *Transit. Met. Chem.* **2008,** *33* (7), 911-919.
49. Kolev, T.; Koleva, B. B.; Zareva, S. Y.; Spiteller, M., Au(III)-complexes of the alanyl-containing peptides glycylalanine and glycylalanylalanine – Synthesis, spectroscopic and structural characterization. *Inorg. Chim. Acta* **2006,** *359* (13), 4367-4376.
50. Koleva, B. B.; Zareva, S.; Kolev, T.; Spiteller, M., New Au(III), Pt(II) and Pd(II) complexes with glycyl-containing homopeptides. *J. Coord. Chem.* **2008,** *61* (22), 3534-3548.
51. Bhattacharjee, R. R.; Das, A. K.; Haldar, D.; Si, S.; Banerjee, A.; Mandal, T. K., Peptide-assisted synthesis of gold nanoparticles and their self-assembly. *J. Nanosci. Nanotechnol.* **2005,** *5* (7), 1141-1147.
52. Lv, P.; Qiu, L.; Zhao, C.; Fang, G.; Liu, J.; Wang, S., Synthesis of Fluorescent Au Clusters Using Self-Assembled Tripeptides as Reducing Soft Templates. *ChemNanoMat* **2019,** *5* (2), 158-162.
53. Ferreira, P. M. T.; Maia, H. L. S.; Monteiro, L. S.; Sacramento, J., Michael addition of thiols, carbon nucleophiles and amines to dehydroamino acid and dehydropeptide derivatives. *J. Chem. Soc., Perkin Trans. 1* **2001,** (23), 3167-3173.
54. Siodłak, D., α,β-Dehydroamino acids in naturally occurring peptides. *Amino Acids* **2015,** *47* (1), 1-17.
55. Amenabar, I.; Poly, S.; Nuansing, W.; Hubrich, E. H.; Govyadinov, A. A.; Huth, F.; Krutokhvostov, R.; Zhang, L.; Knez, M.; Heberle, J.; Bittner, A. M.; Hillenbrand, R., Structural analysis and mapping of individual protein complexes by infrared nanospectroscopy. *Nat. Commun.* **2013,** *4* (1), 2890.
56. Buczek, A. M.; Ptak, T.; Kupka, T.; Broda, M. A., Experimental and theoretical NMR and IR studies of the side-chain orientation effects on the backbone conformation of dehydrophenylalanine residue. *Magn. Reson. Chem.* **2011,** *49* (6), 343-349.
57. Lee, H.-E.; Kim, R. M.; Ahn, H.-Y.; Lee, Y. Y.; Byun, G. H.; Im, S. W.; Mun, J.; Rho, J.; Nam, K. T., Cysteine-encoded chirality evolution in plasmonic rhombic dodecahedral gold nanoparticles. *Nat. Commun.* **2020,** *11* (1), 263.
58. González-Rubio, G.; Mosquera, J.; Kumar, V.; Pedrazo-Tardajos, A.; Llombart, P.; Solís, D. M.; Lobato, I.; Noya, E. G.; Guerrero-Martínez, A.; Taboada, J. M.; Obelleiro, F.; MacDowell, L. G.; Bals, S.; Liz-Marzán, L. M., Micelle-directed chiral seeded growth on anisotropic gold nanocrystals. *Science* **2020,** *368* (6498), 1472-1477.
59. Feng, Z.; Wang, H.; Wang, S.; Zhang, Q.; Zhang, X.; Rodal, A. A.; Xu, B., Enzymatic Assemblies Disrupt the Membrane and Target Endoplasmic Reticulum for Selective Cancer Cell Death. *J. Am. Chem. Soc.* **2018,** *140* (30), 9566-9573.
60. Feng, Z.; Wang, H.; Chen, X.; Xu, B., Self-Assembling Ability Determines the Activity of Enzyme-Instructed Self-Assembly for Inhibiting Cancer Cells. *J. Am. Chem. Soc.* **2017,** *139* (43), 15377-15384.
61. Zhou, J.; Du, X.; Yamagata, N.; Xu, B., Enzyme-Instructed Self-Assembly of Small d-Peptides as a Multiple-Step Process for Selectively Killing Cancer Cells. *J. Am. Chem. Soc.* **2016,** *138* (11), 3813-3823.
62. Pieszka, M.; Han, S.; Volkmann, C.; Graf, R.; Lieberwirth, I.; Landfester, K.; Ng, D. Y. W.; Weil, T., Controlled Supramolecular Assembly Inside Living Cells by Sequential Multistaged Chemical Reactions. *J. Am. Chem. Soc.* **2020,** *142* (37), 15780-15789.

63. Zapadka, K. L.; Becher, F. J.; Uddin, S.; Varley, P. G.; Bishop, S.; Gomes dos Santos, A. L.; Jackson, S. E., A pH-Induced Switch in Human Glucagon-like Peptide-1 Aggregation Kinetics. *J. Am. Chem. Soc.* **2016,** *138* (50), 16259-16265.
64. Wang, H.; Feng, Z.; Del Signore, S. J.; Rodal, A. A.; Xu, B., Active Probes for Imaging Membrane Dynamics of Live Cells with High Spatial and Temporal Resolution over Extended Time Scales and Areas. *J. Am. Chem. Soc.* **2018,** *140* (10), 3505-3509.
65. Chan, K. H.; Lee, W. H.; Ni, M.; Loo, Y.; Hauser, C. A. E., C-Terminal Residue of Ultrashort Peptides Impacts on Molecular Self-Assembly, Hydrogelation, and Interaction with Small-Molecule Drugs. *Sci. Rep.* **2018,** *8* (1), 17127.
66. Larnaudie, S. C.; Brendel, J. C.; Romero-Canelón, I.; Sanchez-Cano, C.; Catrouillet, S.; Sanchis, J.; Coverdale, J. P. C.; Song, J.-I.; Habtemariam, A.; Sadler, P. J.; Jolliffe, K. A.; Perrier, S., Cyclic Peptide–Polymer Nanotubes as Efficient and Highly Potent Drug Delivery Systems for Organometallic Anticancer Complexes. *Biomacromolecules* **2018,** *19* (1), 239-247.
67. Kemper, B.; Hristova, Y. R.; Tacke, S.; Stegemann, L.; van Bezouwen, L. S.; Stuart, M. C. A.; Klingauf, J.; Strassert, C. A.; Besenius, P., Facile synthesis of a peptidic Au(i)-metalloamphiphile and its self-assembly into luminescent micelles in water. *Chem. Commun.* **2015,** *51* (25), 5253-5256.
68. Iglesias, D.; Melle-Franco, M.; Kurbasic, M.; Melchionna, M.; Abrami, M.; Grassi, M.; Prato, M.; Marchesan, S., Oxidized Nanocarbons-Tripeptide Supramolecular Hydrogels: Shape Matters! *ACS Nano* **2018,** *12* (6), 5530-5538.
69. D.A. Case, K. B., I.Y. Ben-Shalom, S.R. Brozell, D.S. Cerutti, T.E. Cheatham, III, V.W.D. Cruzeiro,; T.A. Darden, R. E. D., G. Giambasu, M.K. Gilson, H. Gohlke, A.W. Goetz,R Harris, S. Izadi, S.A. Iz-; mailov, K. K., A. Kovalenko, R. Krasny, T. Kurtzman, T.S. Lee, S. LeGrand, P. Li, C. Lin, J. Liu,; T. Luchko, R. L., V. Man, K.M. Merz, Y. Miao, O. Mikhailovskii, G. Monard, H. Nguyen, A. Onufriev, F.; Pan, S. P., R. Qi, D.R. Roe, A. Roitberg, C. Sagui, S. Schott-Verdugo, J. Shen, C.L. Simmerling, N.R.; Skrynnikov, J. S., J. Swails, R.C. Walker, J. Wang, L. Wilson, R.M. Wolf, X. Wu, Y. Xiong, Y. Xue,; Kollman, D. M. Y. a. P. A. *AMBER20*, University of California, San Francisco, 2020.
70. Birarda, G.; Bedolla, D.; Piccirilli, F.; Stani, C.; Vondracek, H.; Vaccari, L., Chemical analyses at micro and nano scale at SISSI-Bio beamline at Elettra-Sincrotrone Trieste. *SPIE* **2022**, 11957, 1195707.
71. Piccirilli, F.; Tardani, F.; D'Arco, A.; Birarda, G.; Vaccari, L.; Sennato, S.; Casciardi, S.; Lupi, S., Infrared Nanospectroscopy Reveals DNA Structural Modifications upon Immobilization onto Clay Nanotubes. *Nanomaterials* **2021,** *11* (5), 1103.
72. Ruggeri, F. S.; Longo, G.; Faggiano, S.; Lipiec, E.; Pastore, A.; Dietler, G., Infrared nanospectroscopy characterization of oligomeric and fibrillar aggregates during amyloid formation. *Nat. Commun.* **2015,** *6* (1), 7831.